Effect of Li_2O on the structure and properties of low-boron aluminosilicate fiber glasses from molecular dynamics simulations and quantitative structure–property relationship analysis

Wenqing Xie, Hong Li, Daniel R. Neuville, Jincheng Du

Effect of Li_2O on the structure and properties of low-boron aluminosilicate fiber glasses from molecular dynamics simulations and QSPR analysis

Wenqing Xie [a], Hong Li [b], Daniel R. Neuville [c], Jincheng Du [a, *]

[a] College of Engineering, University of North Texas, Denton, TX 76203, USA

[b] Nippon Electric Glass, Shelby, NC, USA

[c] Université de Paris, IPGP-CNRS, Paris, France

* Corresponding author: jincheng.du@unt.edu

Abstract:

Mixed alkaline earth (MgO, CaO) aluminosilicate glass fibers (MCAS) with and without boron are commonly used as reinforcements in plastic composites and the fundamental understanding of the thermal and mechanical properties is essential to the design of new glass compositions to satisfy the growing demands in applications from renewable energy to lightweight structural components. In this work, a series of Li_2O containing low-boron MCAS fiber glasses have been studied by using molecular dynamic (MD) simulations with recently developed effective partial charge composition dependent boron potentials. Structural characteristics such as pair distribution function, bond angle distribution, neutron/X-ray diffraction structure factors were calculated, as well as properties such as elastic moduli and vibrational density of states. The addition of Li_2O was found to improve the elastic moduli of the fiber glasses in excellent agreement with experimental results we reported earlier. The simulation results showed that the weakened network connectivity and decrease of tri-/bridging oxygen have positively affected the lowering of liquid temperature, owing to the transformation to more boron Q^2 and silicon/aluminon Q^3. It is found that higher oxygen packing density, coordinated aluminum/boron species such as $[AlO_5]$ and $[BO_4]$ units, larger-membered oxide rings, and intensified connections of $[AlO_x]$ and $[SiO_4]$ are the main reasons that lead to improved mechanical properties. MD based quantitative structure-property relationship (QSPR) analyses are performed and showed excellent correlations to measured properties, indicating that it is a promising prediction approach for future glass composition design.

Keywords: lithium oxide, boron, network connectivity, QSPR approach, mechanical property.

1. Introduction

Glass fiber-reinforced plastic (GFRP) composites have been widely used in automobiles, wind turbine blades, chemical storage, and others as a lightweight, high strength structural component since they were first introduced in the 1930s.[1, 2] Continuous developments in the past years have produced a variety of reinforcement fiber glass family, such as E-Glass with high electrical resistance, S-Glass with high strength, ECR-Glass with good chemical resistance, and silica glass with low dielectric constants.[3, 4] In particular, E-Glass is a widely used fiber glass composition and commonly contains CaO, Al_2O_3, SiO_2, and (0-10 mol. %) B_2O_3.[5, 6] Subsequently a chemical-resistant ECR-Glass was developed mainly by modifying the B_2O_3 amount and introducing MgO as well as less than 1 mol. % alkali oxide, inspired by the early fabricated C-Glass. The subsequent designation of fiber glass composition is related to specific applications, for example, a high-modulus and high-temperature S-Glass (S2 with elastic modulus of 87-91 GPa) mainly contains MgO, Al_2O_3, and SiO_2 for ballistic protections. For wind turbine blade applications, glass fiber is supposed to have high strength, high stiffness, good chemical durability, and ideally low drawing temperature to ease processing and reduce energy consumption. However, the commonly used E/ECR-Glass fibers only have modest Young's modulus despite their low drawing temperature. Therefore, the R-Glass based on the quaternary system of MgO-CaO-Al_2O_3-SiO_2 (MCAS) and its derivatives were developed to have high mechanical strength with modulus in the range of 95-106 GPa. In the meantime, their liquid temperature (T_{Liq}) can be reduced by introducing B_2O_3 and Li_2O at the expense of MgO which is called HS-Glass fiber, although the T_{Liq} still needs to be further reduced to realize commercial production.[7, 8]

For the fabrication aim of higher modulus and lower T_{Liq} as compared with the E/E-CR glass, R-Glass based MCAS system was studied for further property optimization by using monovalent alkali, [8] divalent alkali earth and transition metal ions,[9] or trivalent rare-earth (RE) ions.[10] Owing to the complicated amorphous glass network, there is no crystal-like periodic structure in simplifying the analysis of arrangements of glass former groups ([SiO_4], [AlO_4], and [BO_3], etc.) that are highly sensitive to the type and amount of other modifier cations.[11-13] 1D/2D nuclear magnetic resonance (NMR) spectra of ^{29}Si, ^{27}Al, and ^{11}B are effectively utilized to analyze non-/bridging oxygen (NBO/BO) distribution, cationic coordination number, and polyhedral connections in the glass. For example, H. Zuo, et al.[9] reported the importance of B_2O_3 for glass viscosity in the system of MgO-CaO-Al_2O_3-SiO_2 with less than 5 mol. % B_2O_3 modified by divalent Ba^{2+} using magic angle spinning nuclear magnetic resonance (MAS-NMR) spectra of ^{27}Al. And the deconvoluted NMR curve quantified the transformation to [AlO_4] at the expense of [AlO_5]

and [AlO_6] as increasing the molarity of B_2O_3. Al_2O_3 intermediate is known for the inhibition of phase separation and network strengthening in the borosilicate and phosphate glasses and the conversions of multi-coordinated [AlO_x] species are highly related to the charge compensation and have impacts on glass viscosity, crystallization, chemical stability, elastic property, coefficient of thermal expansion, density, molar volume, etc.[14-18] Similar to Al_2O_3, the trivalent RE_2O_3 oxides are found to assist in increasing T_g/soft temperature and strengthening glass network in MCAS glass fibers, as well as to affect high-temperature properties that are to decrease melting temperature and depolymerize glasses as glass modifiers by virtue of the low ionic field strength of RE ions proved by 2D MAS-NMR.[10] They deduced that RE_2O_3 oxides were supposed to lower the T_{Liq} and high-temperature viscosity of MCAS glasses in a certain range, plus increase both fiber tensile strength and Young's modulus at the same time. On the other hand, the Vickers hardness was found to have a linear positive correlation with the RE_2O_3 (RE = Y, Lu) constituent and the average coordination number of Al in ternary aluminosilicate glasses, as determined experimentally and computationally by S. Iftekhar, et al. [19] Besides, J. Kalahe, et al. [20] demonstrated a strong enhancement of elastic modulus for the high field strength of yttrium in the Y_2O_3-Al_2O_3-SiO_2 system which was proved by a partial charge dependent molecular dynamics (MD) simulation. As progressively developing on R-glass, an intriguing discovery from the new development of R-Glass is that a small amount of Li_2O introduced in the low-boron containing aluminosilicate glass will benefit on lowering both the glass melt viscosity and liquidus temperatures, while surprisingly improving the Young's modulus. The glass formation details will be demonstrated in another paper comprehensively. Li_2O doped MCAS glasses have attracted lot of attentions for the even lower melting temperature and better Young's modulus, but unfortunately the local glass structures haven't been clarified yet.

Molecular dynamics simulations have become a valuable tool to obtain short and medium range structural features of glass materials.[21-23] Structural information such as network former connectivity and modifier cation local chemical environment in the glass can be obtained from MD simulations.[24, 25] MD simulations of borosilicate glasses are more challenging than the widely studied silicate glasses due to the difficulty to obtain reliable potential parameters to account for the composition dependent boron coordination changes.[26] To compare the potential transferability in MD simulations of borosilicate glasses,[27] Tuheen et al. have compared four widely recognized potentials in modeling Na_2O-B_2O_3-SiO_2 ternary and quartery systems with addition of Al_2O_3. The results showed that Du's potential (developed based on the Teter potential)[28, 29] showed the best

compatibility to the varied molar ratio R=[Na_2O]/[B_2O_3] (0.1 to 4) in comparison to the Dell & Bray Model,[30] while the other potentials[31, 32] presented moderate to strong divergences to the measured fraction of four-fold coordinated boron (^{IV}B). Hinted from the work, the potential development by Deng and Du potential was chosen to simulate the structure of alkali-/alkaline earth ions mixed boroaluminosilicate glasses in this work. Recently, Zeng et al.[33] demonstrated a linear effect of R([MgO]/[B_2O_3]) on the thermal stability and mechanical properties ranging from S-fiber to E-fiber by using Deng and Du's potential, which was proved to be feasibly applied in the research of glass fibers for the good consistency with experimental results.

The study aimed to perform molecular dynamics simulations on a series of boroaluminosilicate glass compositions that were previously studied experimentally. The goal is to determine the structural origin of a mechanical strengthening anomaly in Li_2O-containing boroaluminosilicate MCAS glasses while lowering T_{Liq}. The study also includes the investigation of a composition with Na_2O to Li_2O substitution for comparison.

2. Methodology

The compositions of MCAS aluminosilicate glasses are list in Table 1. The specific glass melting experimentally and heat-treatment processes have been fully descripted in the previous paper.[6, 10] The processing technique of fiber glass and structure-property characterizations will be published separately. Briefly explaining, the glass series are named MCAS with the number postfix from 1 to 8, and the typical MCAS1, MCAS3, MCAS5, MCAS7, and MCAS8 glasses are generated by the method of molecular dynamic simulations. The liquidus temperature, reference temperatures of glass melting (T_{10}) at the viscosity of 10 Pa·s, reference fiber drawing temperature (T_{100}) at 100 Pa·s, and temperature difference ($\Delta T=T_{100}-T_{Liq}$) are cited to analyze and predict the relationships of structure and property using QSPR approach.[34-37] Additionally, the experimental elastic moduli of MCAS glass series will be used to support the results of mechanical properties calculated by MD simulation and to correlate with energy descriptors F_{net}.

For the MD simulation, initial atomic configurations are generated by the LAMMPS software[38] with periodic boundary conditions in a cubic cell randomly distributed with 10,000 atoms. The initial density (ρ_{fib}) and molar volume (V_M, cubic box volume over the total mole) setups are based on the experimental results as listed in Table 1. The MCAS glasses are melt-quenched by a cooling rate of 1 K/ps from 5,000 to 3,500 K with a canonical ensemble with constant number of atoms,

volume, temperature (NVT) for equilibration, then quench to 300 K with an isobaric isothermal ensemble NPT (constant number of atoms, pressure, and temperature) followed with NVT ensemble for 100 ps. Partial charge pairwise potentials consist of a short-range item with modified Buckingham form developed by Deng and Du and a long-range Columbic interaction as reported in the previous paper.[29, 39] The simulated final density (ρ_{fib}') and molecular volume (V_M') are listed in table 1. The glass melt-quench is done on LAMMPS software and the structure is shown as Fig. 1, while the following structure analysis and property calculation are done by in-house programs. Quantitative structure-property relationship approach (as shown in Eq. 1) is utilized to obtain an energetic descriptor (F_{net}) with variables of total number of atoms (N), cation/anion pairs (ij), number of cation species (n_i), mean coordination numbers (CN), single bond strength (SBS), and a multiplicative factor m_x.[40, 41] The diffusion coefficients of cations in MACS glass systems are calculated based on Einstein's equation (Eq. 2) and the internal item of mean square displacement (MSD) can be read from trajectory file and calculated according to Eq. 3. Temperature-dependent atomic diffusions are obtained by ramping up temperature from 300 K to 2,000 K with an interval of 50 K. At each temperature setpoint, the ensembles of NPT Hoover (1.0 1.0) and NVE will be done alternately with 200 ps. The atomic position will be recorded in a trajectory file every 5,000 steps, as published in the previous paper.[42, 43] The vibration spectra are calculated according to the velocity auto-correlation function (VACF) and the vibrational density of states (VDOS). The specific theoretical demonstration and the operation of MD simulation can be referred to the previous paper.[44] Mechanical properties are calculated by the LAMMPS packages based on the elastic constant tensors (C_{ij}) and compliances ($S_{ij} = C_{ij}^{-1}$), obtained by exerting a finite deformation of 0.5 %. The corresponding relationship of stress (δ) and strain (ε) are shown in Eq. 6. The bulk and shear moduli are calculated based on Voigt and Reuss methods, and the Young's modulus will be obtained by the Hill's method, which is the geometric average of the Voigt and Reuss methods. The specific theories and operations can be referred to the papers.[45-47]

$$F_{net} = \frac{1}{N}\left[\sum_i^{cations}\sum_j^{anions} n_i \cdot CN_{ij} \cdot SBS_{ij} \cdot M_{ij}\right] \quad (1)$$

$$D = \frac{1}{6}\lim_{t\to\infty}\frac{<\vec{r}(t)>^2}{t} \quad (2)$$

$$<\vec{r}(t)^2> = \frac{1}{N}\sum_{i=0}^{N}(\vec{r}_i(t) - \vec{r}_i(0))^2 \quad (3)$$

$$c(t) = \langle v(t) \cdot v(0)\rangle / \langle v(0) \quad (4)$$

$$f(x) = \frac{2}{\pi}\int_0^{\infty} C(t)\cos\omega t\, dt \tag{5}$$

$$\delta_i = C_{ij} \times \varepsilon_j \tag{6}$$

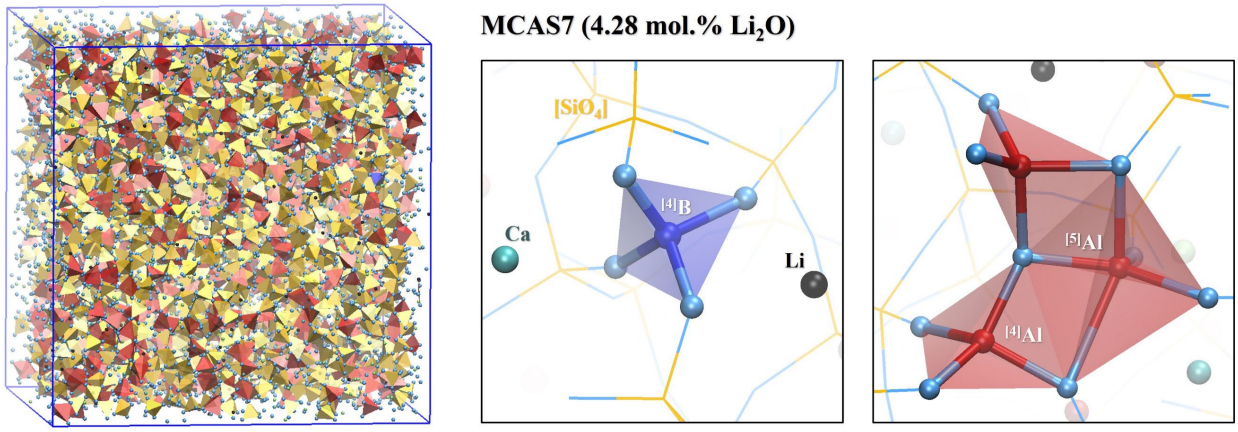

Figure 1. MCAS7 glass configuration; O-light blue, Si-yellow, B-blue, Al-red, Mg-lime, Ca-cyan, Li-black.

Table 1. Compositions (mol. %), molar volume (cm^3/mol) and density (g/cm^3) in MCAS glasses.

	SiO_2	Al_2O_3	B_2O_3	CaO	MgO	Li_2O	Na_2O	V_M	V_M'	ρ_{fib}	ρ_{fib}'
MCAS1	60.37	14.45	0.83	8.31	16.05	0.00	0.00	7.919	8.042	2.544	2.584
MCAS2	59.32	14.48	0.83	8.32	16.08	0.97	0.00	-	-	-	-
MCAS3	57.00	14.05	0.00	12.31	15.35	1.30	0.00	7.820	8.019	2.575	2.640
MCAS4	58.29	14.50	0.83	8.34	16.11	1.93	0.00	-	-	-	-
MCAS5	58.61	14.30	0.82	8.22	15.88	2.16	0.00	7.888	7.934	2.554	2.579
MCAS6	57.58	14.33	0.82	8.24	15.92	3.11	0.00	-	-	-	-
MCAS7	56.89	14.16	0.81	8.14	15.72	4.28	0.00	7.720	7.900	2.537	2.596
MCAS8	56.89	14.16	0.81	8.14	15.72	0.00	4.28	7.926	8.079	2.537	2.585

3. Results

Pair distribution function reflects the nearest non-/bridging oxygen (NBO/BO) around cations in glasses. The corresponding cut-off distance is an important parameter to calculate the averaged coordination number of cation-oxygen pairs, as shown in Fig. 2. It can be observed that those glass former cations present strong covalent bonds to oxygen and are located at low distance positions with sharp peaks. In contrast, the modifier cations have lower interaction with oxygens and are usually with wide FWHM located at long atomic distances. In general, the first minimum point at the down curve will be read as the cut-off distance for further structure analyses. For example, the cut-off is expected to yield the total distribution function (TDF) and averaged CN as shown in Fig. 2c.[48] There are apparently flat plateaus on the CN curves of Si-O, B-O, and Al-O, while the glass modifier cations present higher CN with oxygens presenting features of ionic bonds, as concluded

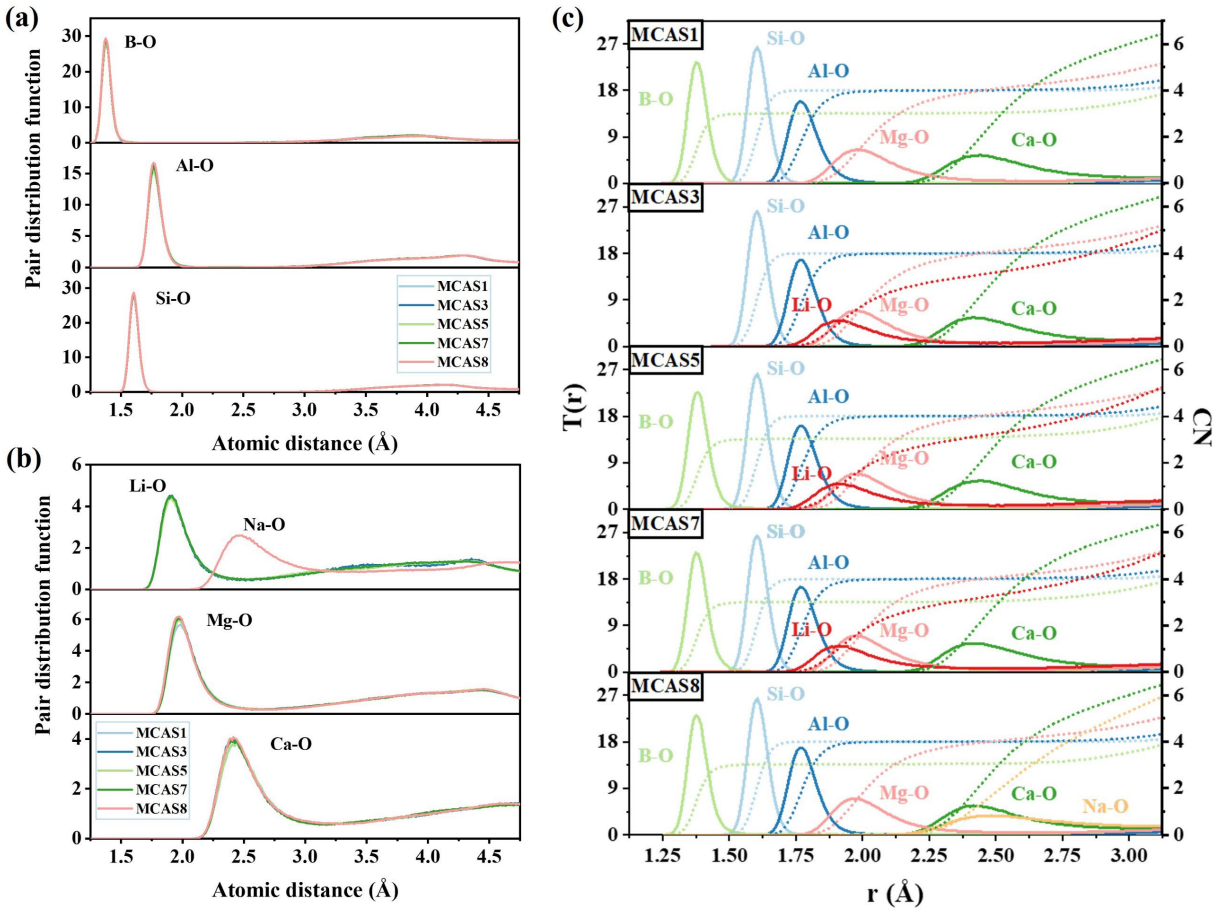

Figure 2. (a-b) Pair distribution function of glass formers and glass modifiers. **(c)** Total correlation function and average coordination number.

in Table 2. The simulation reproduced good four-fold coordinated [SiO_4] units with hundred percentage while the high-fold [AlO_5] and [BO_4] species was found in the network along with the trigonal [BO_3] and tetrahedral [AlO_4]. The result can be easily visualized as the glass structure of MCAS7 shown in Fig. 1. The local connections of [BO_4] to the [SiO_4] groups as well as the charge compensation with cations are observed. Additionally, a five-fold coordinated [AlO_5] group shares edges with two [AlO_4] groups and they connect to each other through a tricluster oxygen. The dense-packed local area shows a two-membered Al-O ring comprising from edge-sharing [AlO_5] and [AlO_4] units. The specific distributions of coordination number and corresponding non-/bridging oxygen are shown in subsequent content.

Table 2. Averaged coordination numbers and cut-off distance for atomic pairs.

Pair/ cut-off (Å)	**Coordination number (Ave.)**				
	MCAS1	**MCAS3**	**MCAS5**	**MCAS7**	**MCAS8**
Si-O /2.20	4.00	4.00	4.00	4.00	4.00
Al-O /2.40	4.01	4.01	4.01	4.01	4.01
B-O /1.85	3.01	-	3.03	3.02	3.03
Na-O /3.45	-	-	-	-	6.23
Ca-O /3.20	5.94	6.01	6.02	5.98	6.03
Li-O /2.48	-	3.19	3.20	3.26	-
Mg-O /2.62	4.05	4.05	4.05	4.05	4.05

Bond angle distribution (BAD) and distribution of total rings are displayed in Fig. 3. It can be observed that [SiO_4] and [BO_3] groups have narrow BADs that are centered at 108.25 and 120.25 degrees respectively, while the [AlO_4] intermediates have relatively broader full wide at half maximum (FWHM) at a vertex of 106.75 degrees. These results are consistent to the previous findings.[49, 50] However, there is a slight peak shift of [AlO_4] units towards high-angle direction when replacing lithium with sodium, which is closer to the theoretical angles of a tetrahedron. In contrast, there is no apparent shift of bond angle distributions in lithium non-/containing glasses whether in the unit of glass formers ([SiO_4], [BO_3]) or glass intermediates [AlO_4]. As the inset graph shown in Fig. 3a, the Al-O-Al angles show a main peak at 120.74 degrees in MCAS1 and a second minor peak at 90.21 degrees which is deem as the existence of [AlO_5] groups.[20, 51] On the other hand, the distribution of glass modifiers surrounding formers are supposed to profile medium range structures. As shown in Fig. 3b-c, the replacement of lithium with sodium leads to a nonnegligible change of chemical environments of [SiO_4] and [AlO_4] groups. The higher

distribution of Al-O-Mg linkages at 88.75 degrees in MCAS1 demonstrate that the addition of Li^+/Na^+ will partially limit the distribution of bond angles and there might be a preferential distribution between Li^+/ Na^+ and Mg^{2+} ions. It is difficult to trace [BO_3] linkages with Li^+/Na^+ in low concentrations by the bond angle distribution. The ring size distribution is shown in Fig. 3d to present the rigid connections of [SiO_4], [BO_x], and [AlO_x] units as increasing the content of alkali ions. The total number of rings decreases monotonically as Li ions increase, and the sodium alternative will even favor the decrease of total ring numbers in MCAS8. In order to assess the ability of glass formers to connect, the average sizes of multiple-membered rings are calculated. MCAS7 glass has the highest average ring member of 8.04 while the sodium alternative (MCAS8) has 7.95. Specifically, the mean ring size will be correlated to the thermal and elastic properties in the subsequent content.

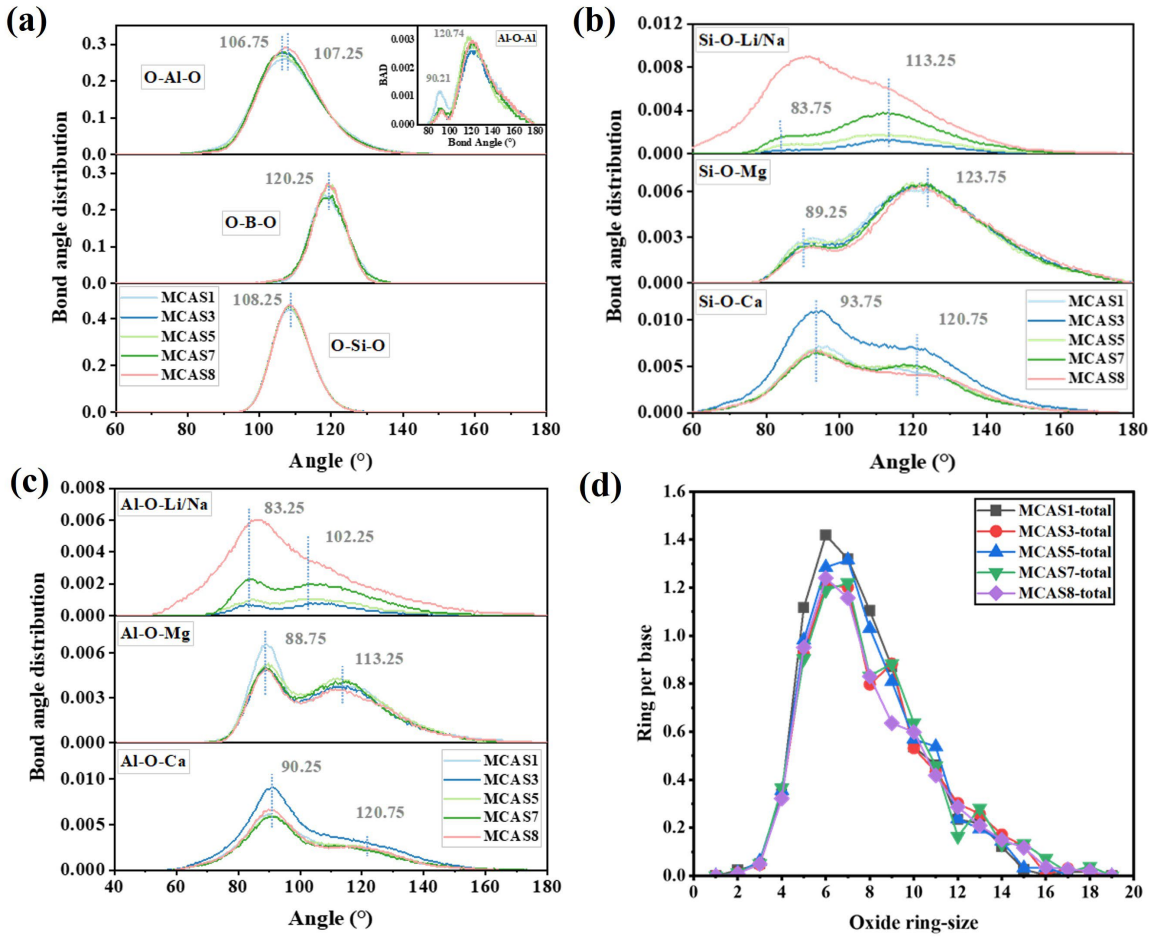

Figure 3. Bond angle distributions of the glass former units **(a)**, and the connections to the modifiers **(b-c)**. **(d)** Ring size distributions of total oxide rings.

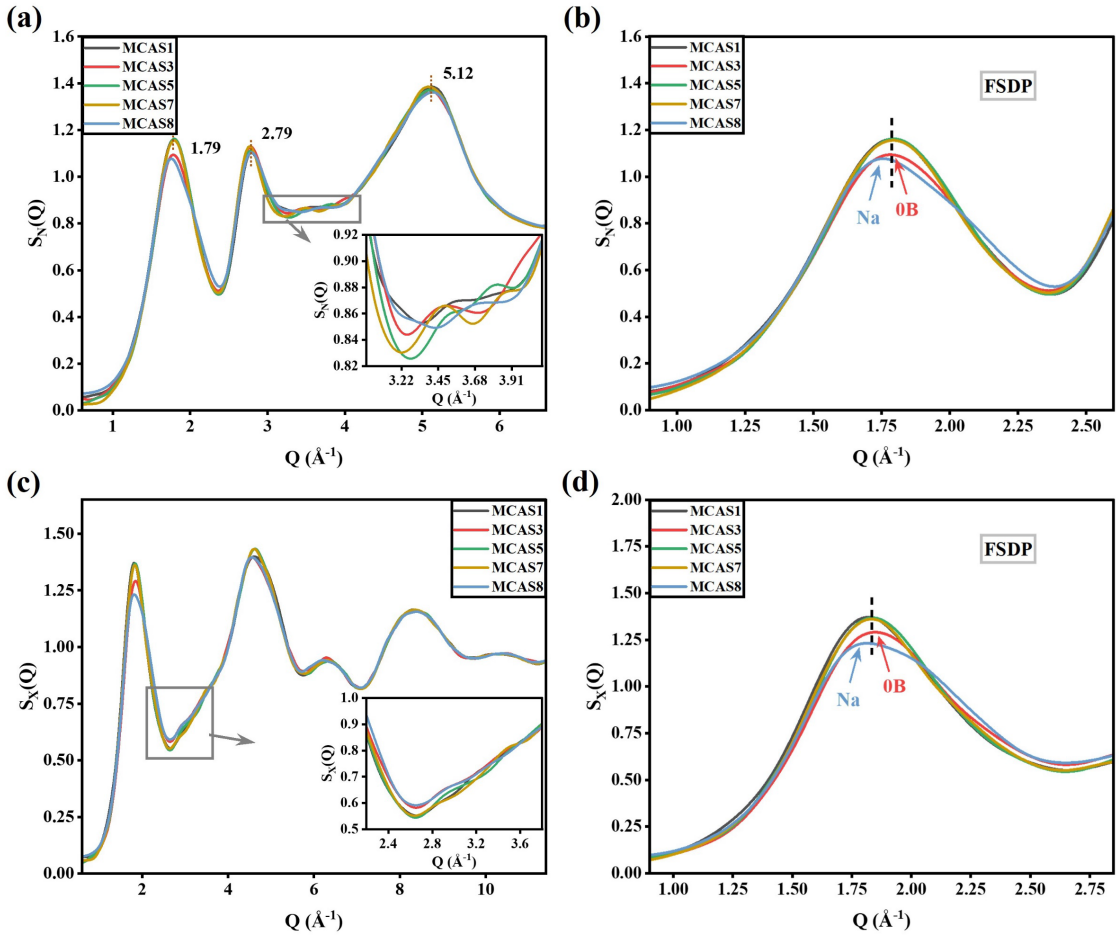

Figure 4. Simulated neutron and X-ray diffractions of MCAS glass series. **(a-b)** Structure factors calculated by neutron diffractions. **(c-d)** Structure factors calculated by X-ray diffractions.

The MD simulation provides atomic scale configurations of MCAS glasses containing middle-/short-range structures that can be functionally characterized by neutron and X-ray diffractions. To deeply understand, the dynamic structural factors of $S_N(Q)$ and $S_x(Q)$ are calculated to give specific information of atomic pairwise and multiple interactions between glass former species (Fig. 4). First sharp diffraction peaks (FSDP) extracted from neutron diffraction are commonly seemed as an effective way to read medium range structures in total scattering patterns of glasses, as shown in Fig. 4b. With the increase of lithium ions, the boron-containing MCAS1, MCAS5, and MCAS7 glasses show overlapped patterns whether at the vertex or FWHM with the increase of lithium, but the MCAS3 with zero boron presents the $S_N(Q)$ intensity decrease. Widely accepted that the FSDP reflects the density fluctuations of pairs in the medium-range scale caused by the directional bonds,[52, 53] thus the calculated FWHM can be a possible tool to analyze network ordering. As presented in Fig. 3b, the replacement of lithium with sodium in MCAS8 widens the

FSDP which signals more disordered and flexible structures. According to Salmon's model, the repeating spaces can be calculated from FSDP based on the formula $d=2\pi/Q$ which means the medium range periodicities.[54, 55] The smaller Q positions, the longer the d-length it will be. Therefore, the poorer periodicity will be observed in the MCAS8 glass compared with these lithium-containing glasses. It's worthwhile to mention that the first sharp diffraction peak obtained from X-ray diffraction (Fig. 4d) similarly presents a trend to the neutron results.

The temperature-dependent self-diffusion coefficients of MCAS7 and MCAS8 are calculated according to the mean-square displacement of lithium and sodium ions (Eq. 2 and Eq. 3), as shown in Fig. 5a-b. The corresponding activation energy can be calculated by Arrhenius equation.[42, 44] It can be known that lithium ions show a better mobility with faster diffusion coefficients over temperature steps, suggesting a more flexible hoping mechanism than the sodium containing MCAS8 glass, which is consistent with literatures.[56-58] What's more, the orders of magnitude in absolute terms are in line with the literature, as shown with iron silicates.[59] The intersection of high- and low-temperature diffusion coefficients yields the glass transition temperature through linear fitting. The lower glass transition temperature of MCAS7 presents the same trend of experimental liquid temperature. Similar to the analysis of atomic displacements, atomic vibrational density of states of MCAS7 and MCAS8 glasses are plotted in Fig. 4c-d according to the velocity auto-correlation function as shown in Eq. 5c-f. There are three main regions for recording total and partial VDOS and the vibration modes of Si and Al atoms are compared with the normalized total Raman spectra. The first region is centered at a broad peak of 159 cm^{-1}, which is attributed to the vibration of all atoms, especially those of the modifiers.[39] The partial VODS of boron is hard to be traced since the minor amount in the glass. However, the vibration information of Si and Al are strongly activated at the middle wavelength region. It can be observed that the partial VDOS of silicon exhibits three main characteristic peaks at 651, 815, and 945 cm^{-1}, respectively, attributed to Si-O rocking/bending vibrations and [SiO_x] groups. For the alumina intermediates, there is an apparent broader peak assigned the Al-O-Al linkages centrally located at 475 cm^{-1} and the stretching mode at 775 cm^{-1}.[60] The simulated partial VDOS of Al and Si atoms are greatly consistent with the experimental Raman shift curves, especially for the Al atoms at 475 cm^{-1} and 775 cm^{-1} as well as the Si atoms at 978 cm^{-1}, as shown in Fig. 5e-f. The third region is located at a broad peak that is centered at 978 cm^{-1} on the total VDOS curve which is mainly contributed by the vibration of oxygen and silicon.

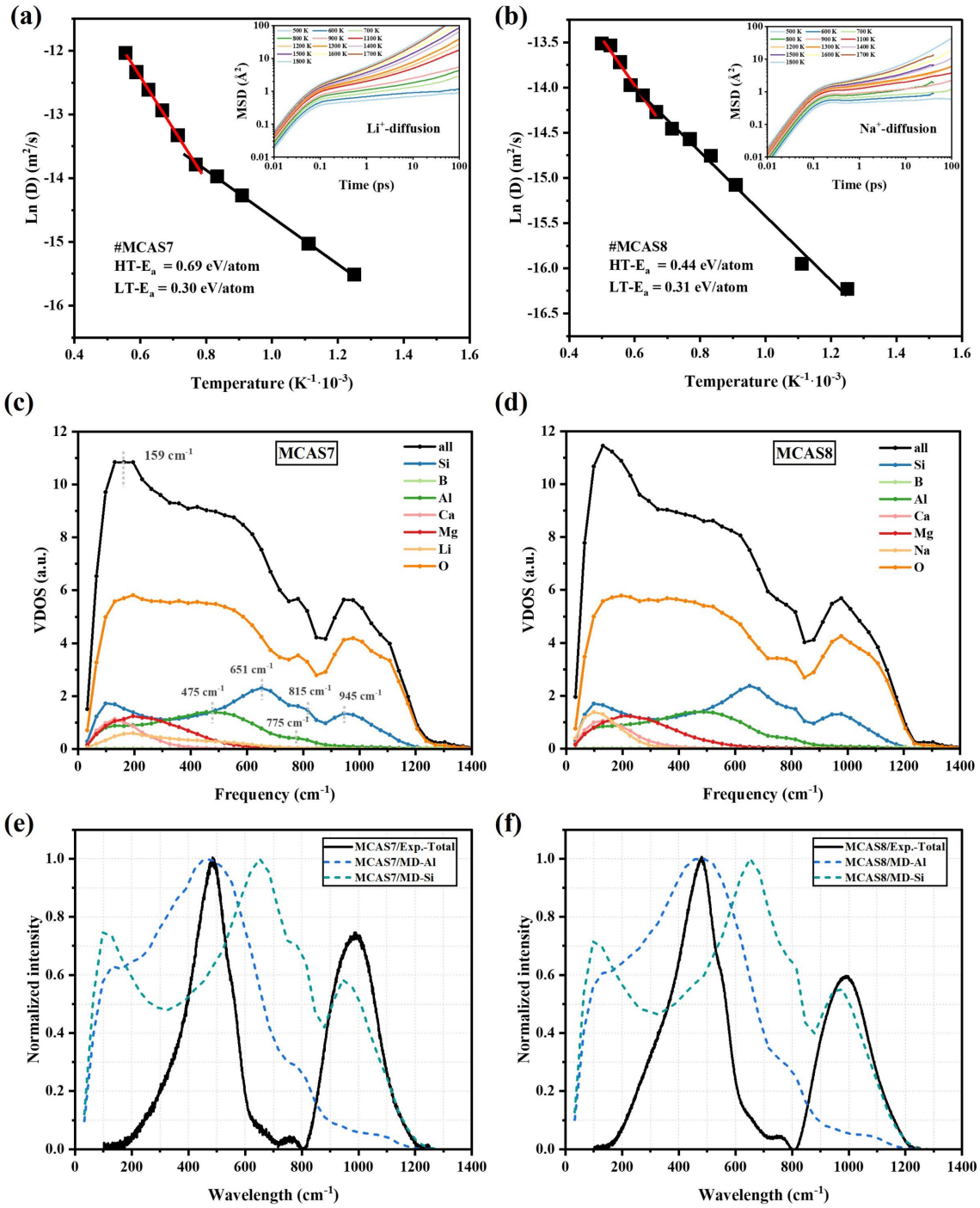

Figure 5. (a-b) Diffusion coefficients of Li-ions and Na-ions as a function of temperature in MCAS7 and MCAS8 glasses. The inset graph is the mean spare displacement as a function of time and temperature. **(c-d)** Total and partial VDOS calculation for MCAS7 and MCAS8 glasses. **(e-f)** Normalized Ramen spectra compared with the normalized partial VDOS of Si and Al atoms in MCAS7 and MCAS8 glasses.

The simulated mechanical properties are calculated in Table 3. The result shows that the

addition of lithium will increase bulk, shear, and Young's modulus, particularly getting the highest bulk modulus at Li_2O content of 4.28 mol. %. In the study, it was found that the Li_2O at 2.16 mol. % possesses the best shear and Young's modulus, both of which are slightly higher than the glass MCAS7 (4.28 mol. % Li_2O). The observed changes in mechanical properties are consistent with experimental results, although the best Young's modulus in the experiment was found to belong to MCAS7. Therefore, the simulated glass modulus can be considered reasonable and reliable for comparison purposes. The results obtained from the MD simulation of MCAS glasses show a peculiar phenomenon where the glass modulus increases with increased Li_2O content and reaches its maximum at a Li_2O concentration of 4.28 mol. % but its liquidus temperature goes reversely, as observed in the experimental results. This phenomenon is particularly pronounced in the simulated bulk modulus.

Table 3. Calculated mechanical properties of MCAS glass series, network connectivity, and the averaged ring size.

ID	**MCAS1**	**MCAS3**	**MCAS5**	**MCAS7**	**MCAS8**
Bulk (GPa)	61.16	62.98	65.39	66.07	61.18
Shear (GPa)	35.96	35.27	36.20	35.88	34.35
Young's (GPa)	90.20	89.15	91.68	91.13	86.79
Poisson ration	0.25	0.26	0.27	0.27	0.26
Network connectivity	3.45	3.32	3.39	3.34	3.34
Mean ring size	7.66	8.02	7.78	8.04	7.95
F_{net} (Kcal/mol)	518.75	504.86	509.02	499.25	499.55

4. Discussion

The analysis of oxygen species is essential to evaluate mechanical properties according to the Makishima and Mackenzie equation ($\boldsymbol{E} = 2V_t \sum_i G_i X_i$), where the E is calculated Young's modulus (GPa), V_t is atomic packing fraction (APF), G_i is dissociation energy per unit volume of component i, and X_i is mole fractions.[12, 53, 61, 62] Herein, oxygen parking density is calculated by the number of oxygens per unit volume (mole per liter),[44] as shown in the Fig. 6a. The result indicates a significant difference between the lithium-containing glasses and both the zero boron (MCAS3) and sodium-substituted samples (MCAS8). As it well known, packing density is highly relative to the glass mole volume and coordination numbers of cation ions and oxygen. The much smaller OPD in sodium containing glass demonstrate a volume expansion compared with the sample containing 4.28 mol. % Li_2O, which suggests a decrease of coordination numbers. The

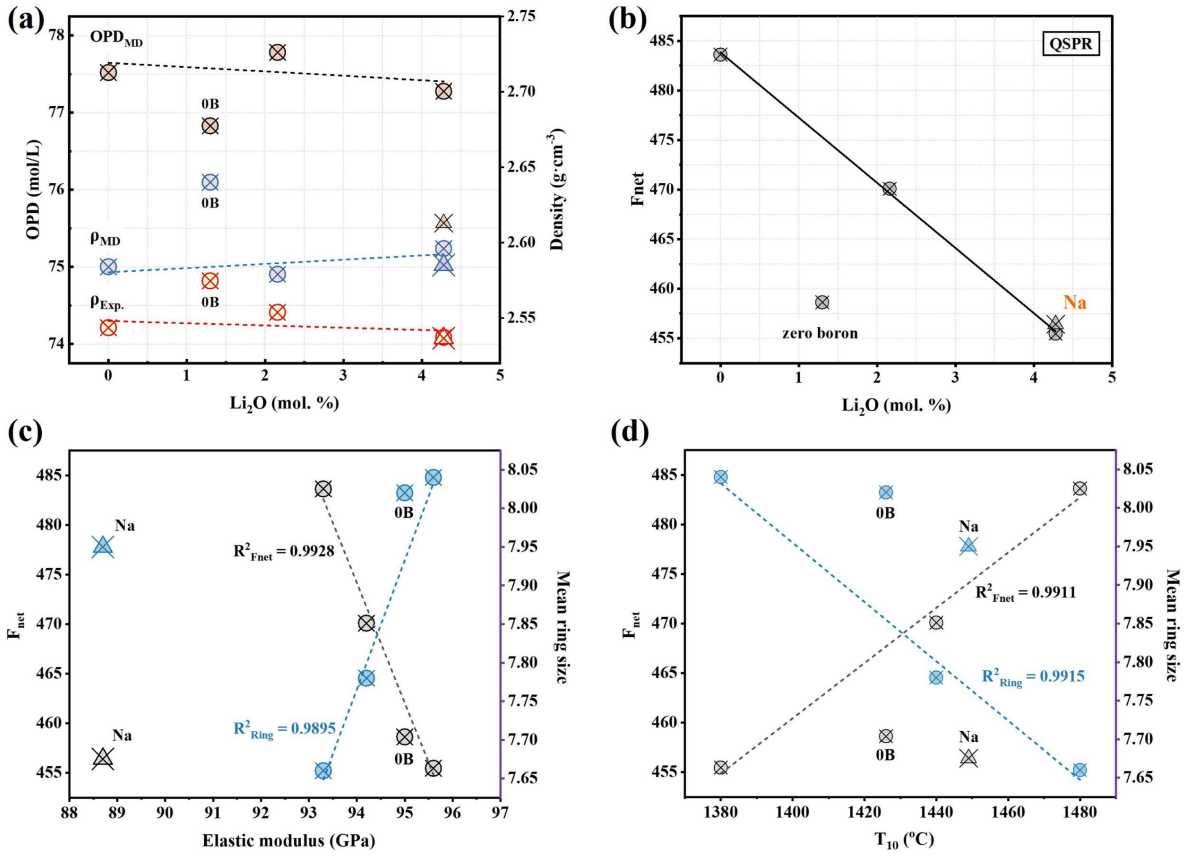

Figure 6. (a) Calculated oxygen packing density and glass densities from both experiment measurements and simulations. **(b)** Energy descriptor F_{net} versus the contents of Li_2O. **(c-d)** The correlation of experimental elastic modulus and T_{10} to the simulated F_{net} and averaged ring size. MCAS8 glass with Na-ions instead of Li-ions is marked trigonal.

result shows that Si is entirely four-fold coordinated to oxygen in the glasses (Table 2), however, the competitive coordination numbers of [BO_x] and [AlO_x] units have vital effects on the physical properties of glasses, as shown in Fig. 7a-b. The glass with no Li_2O has the highest percentage [BO_3] and few [BO_4] units, while the [BO_4] units will be increased with the increase of Li_2O at the expense of [BO_3] units. And the highest point of transformation occurs at a Li_2O content of 2.16 mol. %. However, at a higher Li_2O concentration, the transformation is retarded, while the substitution of Na_2O for Li_2O is shown to accelerate the transformation from [BO_3] to [BO_4] units. On the other hand, the Al-O coordination changes in [AlO_x] units are more complicated, the speciation reactions or transformations of which can be detailed as follows. Based on the MD simulations, the increase in Li_2O results in the increase of [AlO_5] units continuously (Fig. 7b). However, for the cases of Li_2O below 2.16 mol.%, the MD simulations also reveal that both [AlO_4]

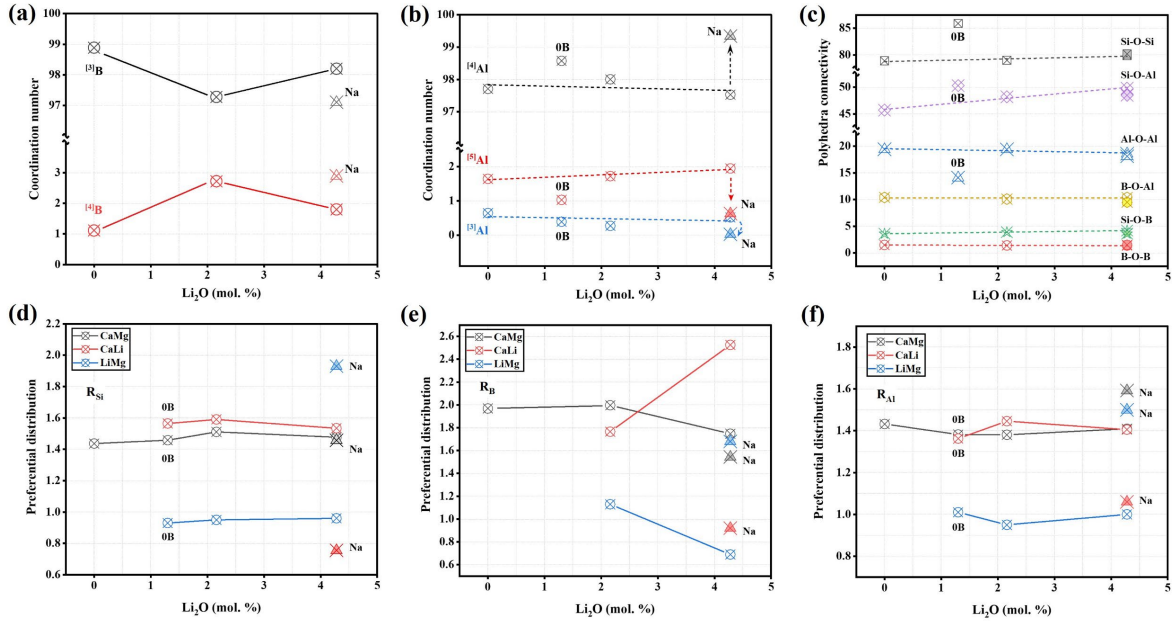

Figure 7. (a-b) Coordination number of B-O and Al-O species. **(c-e)** Preferential distributions of alkali and alkaline earth cations against glass formers. **(f)** Distributions of polyhedral linkages. MCAS8 glass with Na-ions instead of Li-ions is marked trigonal.

and [AlO_5] increases at the expense of [AlO_3] units. At higher Li_2O levels, [AlO_3] unit increase again at the expense of [AlO_4] unit. This competitive transformation at a Li_2O content of 4.28 mol. % will show an increase of high-fold coordinated [AlO_5] and a consumption of [AlO_3] and [AlO_4] units in the end, compared with MCAS1 glass without Li_2O.

It is worth analyzing the sodium-substituted glass MCAS8 since the result shows that [AlO_4] is highly concentrated at the expense of [AlO_3] and [AlO_5] units (Fig. 7b). Additionally, sodium ions are believed to form $[AlO_4]^-$ $[Na]^+$ groups to achieve local charge neutrality for the aluminum-oxygen anions. The present high-fold coordination numbers in [BO_x] and [AlO_x] units are expected to densify atomic packing density and enhance elastic modulus ultimately. Moreover, there is a stronger Li-O bond (144 Kcal) [40] with higher dissociation energy than Na-O bonds (120 Kcal) [40] which can be another reason for the higher Young's modulus in lithium-containing glasses The third point in consideration is that the middle-range structure of the glass series. Besides oxygen packing density, the averaged ring-sizes are also highly positively correlated with the Young's modulus, as shown in Fig. 6c. It can be observed that this glass series should have averaged oxide rings at the eight-membered ring. The glasses, with either zero boron or 4.28 mol. % Li_2O, are closer to the eight-membered averaged oxide ring and exhibit better Young's modulus compared

to those that deviate from eight. Thus, the higher dissociation energy of Li-O bonds, higher atomic packing density, and higher averaged oxide ring size provide coherent reasoning for MCAS7 glass exhibiting higher Young's modulus. Furthermore, lowering both connectivity and bridging oxygen distribution might cause its lower liquid temperature.

The glass modifiers are further studied by analyzing the local environments of glass formers (Si, B, and Al). Specifically, the preferential distributions of the modifiers are calculated in terms of the ratio of the nearest coordination number of one modifier cation against another surrounding each glass former ($R = CN_{(former\text{-}Li)}/CN_{(former\text{-}Mg)} \times n_{Mg}/n_{Li}$). R_{Si}, R_B, and R_{Al} are calculated as the CN ratios of former-modifier pairs and the calculation follows the sequence of CN_{Ca} to CN_{Mg}, CN_{Ca} to CN_{Li}, and CN_{Li} to CN_{Mg}, as shown in Fig. 7c-e. The R-value greater than 1 implies that the prior cation (in the nominator) should be preferentially bonded with the given glass former over the latter (in the denominator). It can be observed that Ca ions always preferentially surround [SiO_4] and [BO_x] glass formers and [AlO_x] intermediates compared to Mg ions. Although Si-O pairs remain four-fold CN in both lithium- and sodium- containing glasses, the change of the local chemical environment occurs when Li ions are substituted by Na ions. The situation is similar to the [BO_x] and [AlO_x]. For the CN_{Ca} to CN_{Li}, R_{Si} and R_{Al} are greater than 1 and present only fair differences when the content of Li_2O is increased. Thus, calcium ions (Ca^{2+}) are more likely to compensate charges for glass formers (Si, B, and Al) compared to lithium ions. However, substituting lithium ions with sodium ions shows varying degrees of influence impact on the local environments of Si, B, and Al. According to the much decreased R_{Si} (less than 1), sodium ions (Na^+) present more preferential coordination to the [SiO_4] and [BO_x] glass formers compared with calcium (Ca^{2+}). While there is a R_{Al} greater than but close to 1 when comparing Ca and Na which means Ca is more likely to compensate charges around [AlO_x] glass intermediates. For the demands of two positive charges to neutralize, the R_{Al} of Ca to Na and Li might suggest the existence of [AlO_5]. Additionally, Mg^{2+} ions are more likely to be localized around Si-O than Li^+ ions and show few differences of R_{Al} as increasing Li_2O. However, a big gap shows on R_B as increasing Li_2O from 2.16 mol. % to 4.28 mol. %. Li ions preferred distribution changes to Mg^{2+} preferred. Additionally, Na^+ ions are always more likely to be localized around Si, B, and Al. Thus, a Rank of $Na^+ > Ca^{2+} > Mg^{2+} > Li^+$ can be given for the preferential distribution around [SiO_4] and [BO_x] units according to MCAS7 and MCAS8, and a different rank of $Ca^{2+} > Na^+ > (Mg^{2+} = Li^+)$ for [AlO_x] units. The polyhedral connectivities of [SiO_4] and [AlO_x] units are depicted in Fig. 7c. It can be observed that increasing Li_2O content will increase the polyhedral connectivity of Si-O-

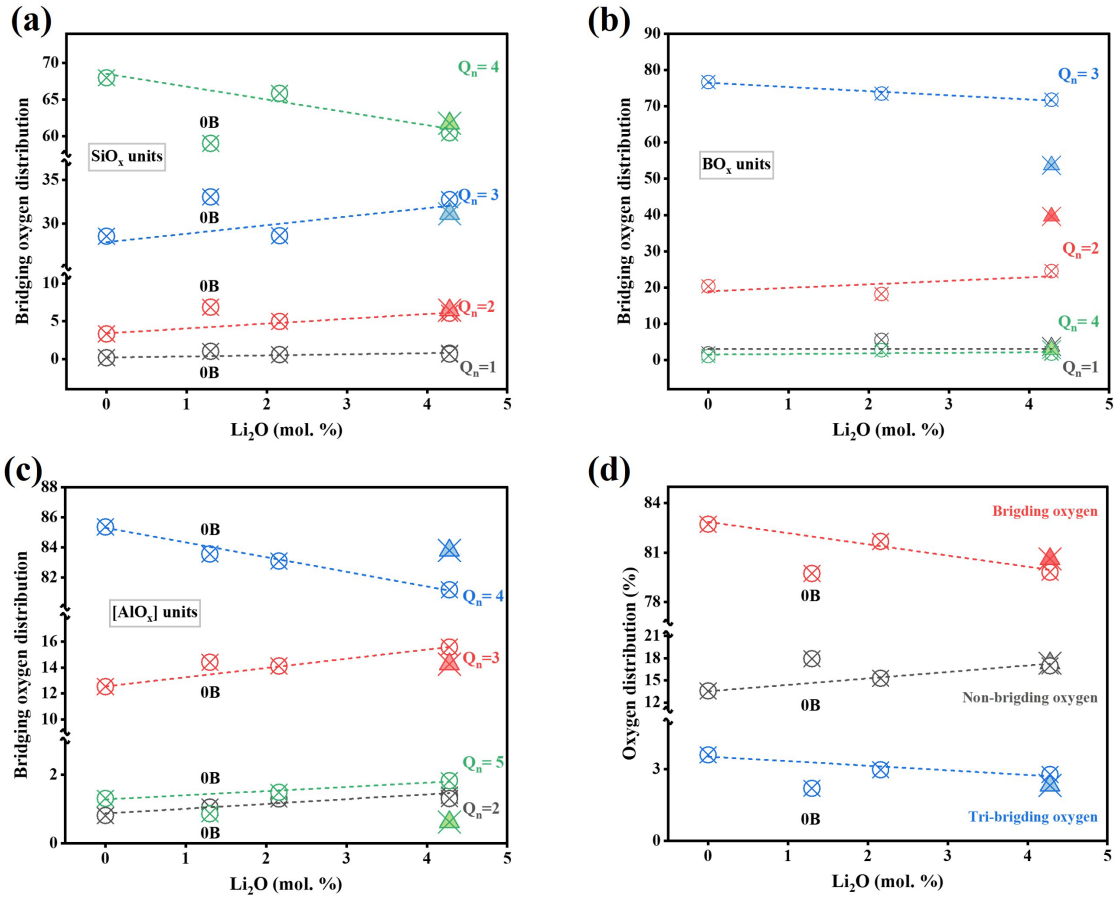

Figure 8. (a-c) Distributions of Q^n species corresponding to [SiO_4], [BO_x], and [AlO_x] units. **(d)** Distributions of oxygen species. MCAS8 glass with Na-ions instead of Li-ions is marked trigonal.

Si, Si-O-B, and Si-O-Al linkages, and the B-O-B and B-O-Al linkages almost remain in the same levels, while the Al-O-Al connectivity will decrease. However, substituting Na ions with Li ions weakens the connectivity of Si-O-B, Si-O-Al, B-O-Al, and Al-O-Al, while slightly strengthening Si-O-Si and B-O-B linkages. Thus, the strengthened connections of Si-O-Si, Si-O-B, and Si-O-Al linkages, the formation of more and higher-fold coordinated [BO_4] and [AlO_5], and small molecular volume (Table 1) might be the reasons for the increased bulk modulus when the Li_2O content is increased.

The non-/bridging oxygen distributions in [SiO_4], [BO_x], and [AlO_x] units offer significant insights into the anomaly of Li_2O enhancement effects on mechanical properties and its inhibition effects on thermal properties (Tg, T_{10}, T_{100}) in the meantime. As shown in Fig. 8, the removal of B_2O_3 in MCAS3 glass will induce more nonbridging oxygens to the [SiO_4] units and produce more $^{[4]}Si$ Q^2 and $^{[4]}Si$ Q^3 at the expense of Q^4 species. Similarly, with increasing contents of Li_2O, Q^2

and Q^3 species in [SiO_4] and [AlO_x] units increase at the expense of Q^4. The aluminon Q^n species herein are the averaged Q^n value from total aluminon-oxygen species, not assigned to the specific coordinated aluminon. In particular, Q^5 species in [AlO_5] units show an increase. This trend will reach a maximum when the concentration of Li_2O is 4.28 mol. %. However, the substitute of Li_2O by Na_2O will lower the transformations in [AlO_x] units when $Al_2O_3/Na_2O > 1$ as the case in our study, which implies sodium is more preferred to be a charge compensator of [AlO_4] units, while lithium is more likely to generate nonbridging oxygen with more Q^2 and Q^3 species in [SiO_4] units. Therefore, the network connectivity and energy descriptor F_{net} (Eq. 1) are expected to decrease as Li_2O increases since the main framework in the glass system are [SiO_4] and [AlO_4] units, as shown in Fig. 7. On the other hand, at the low B_2O_3 level in the glasses (0.81 ~ 0.83 mol. %), its effect shows great importance to the glass structure and property. The trigonal connection of boron [BO_3] and oxygen is the main coordination in [BO_x] family with a small amount of [BO_4]. While the boron Q^n species preferentially transfer to Q^4 and Q^1 at the expense of Q^3 and Q^2 species as increasing Li_2O contents in the range of 0 to 2.16 mol. %. However, the total boron Q^2 species will be largely increased when more Li_2O is added to the composition, meanwhile, its Q^4, Q^3, and Q^1 species will be depleted. The boron Q^n species herein are the averaged Q^n value from total boron-oxygen species, not assigned to the specific coordinated boron. And the transformation intensifies upon replacing lithium with sodium at a Li_2O content of 4.28 mol.%. There is a peak located at 770 cm^{-1} in the Raman spectrum that might be assigned to the B-O rings connected by one [BO_4] and two [BO_3] units. And the deconvolution results suggest a peak decay at high Li_2O content. Although there might be an overlap curve from Al-O stretching mode of Q^3 and Q^2 species, MD results show an increase trend of both aluminon Q^3 and Q^2 transformation. Therefore, the fluctuation at 2.16 mol. % Li_2O and the descending trend of deconvolution peaks at 770 cm^{-1} in experiments are more likely to suggest the formation of boron Q^2 species by considering the experiment and MD results. To sum up, the Q^2 preferred B-O connection and Q^2/Q^3 preferred Si-O/Al-O connections decrease the network connectivity defined as the average quality of bridging oxygens that also plays a role in systematic energy descriptor F_{net} as the multiplicative factor term calculated by averaging the network connectivity of the glass formers (Table 3). Therefore, the decreased network connectivity might be one reason for the lower glass liquidus temperature when increasing the concentration of Li_2O as the linear relationship of F_{net} and T_{10} in Fig. 6d. The idea can also be proved by the decrease of bridging oxygen and tricluster oxygen as well as the increase of non-bridging oxygen in total as oxygen species analysis in Fig. 8d.

5. Conclusions

In this work, a series of Li_2O-containing MCAS glasses is modeled by the molecular dynamic simulations (MD). The Young's modulus trend calculated by the MD simulations closely mimic the positive effect of Li_2O on Young's modulus obtained from experimental study. Furthermore, the MD results also supports the functional role of Li_2O in decreasing liquidus (T_L), glass melting (T_{10}), and fiber forming temperatures (T_{100}). The glass configurations are demonstrated by the calculation of atomic pair distribution, averaged coordination of pairs, bond angle distribution, neutron/X-ray diffraction, and atomic vibrational density of states. The Lower distribution of averaged boron Q^n and $^{[4]}Si$ Q^n species induced network connectivity exhaustion that further proved by QSPR approach is considered as the main reason for the decreased glass liquid temperature with the increase of Li_2O. Additionally, the decreased distribution of tri-/bridging oxygen is considered as another reason for lowering liquid temperature. The analyses of oxygen packing density, dense packing of more and higher-coordinated $[BO_4]$ and $[AlO_5]$ units, and the formation of higher membered oxide ring suggest the monotonically enhanced Young's modulus. The energetic descriptors from QSPR approach and averaged ring size are linearly correlated to the thermal and mechanical properties, presenting a promising prediction for future structure optimizations.

Acknowledges

The authors thank the Research Computing Services, a division under the Office of Research and Innovation at the University of North Texas, for providing TACC computational and data analytics resources that have contributed to the research results reported within this paper.

References

1. Li, H.; Charpentier, T.; Du, J.; Vennam, S. Composite reinforcement: Recent development of continuous glass fibers. *International Journal of Applied Glass Science* **2017**, *8* (1), 23-36. DOI: 10.1111/ijag.12261.
2. Li, H. *Fiberglass Science and Technology*; 2021. DOI: 10.1007/978-3-030-72200-5.
3. Zhang, M.; Matinlinna, J. P. E-Glass Fiber Reinforced Composites in Dental Applications. *Silicon* **2011**, *4* (1), 73-78. DOI: 10.1007/s12633-011-9075-x.
4. Cousins, D. S.; Suzuki, Y.; Murray, R. E.; Samaniuk, J. R.; Stebner, A. P. Recycling glass fiber thermoplastic composites from wind turbine blades. *Journal of Cleaner Production* **2019**, *209*, 1252-1263. DOI: 10.1016/j.jclepro.2018.10.286.

5. Reben, M.; Li, H. Thermal Stability and Crystallization Kinetics of MgO-Al_2O_3-B_2O_3-SiO_2 Glasses. *International Journal of Applied Glass Science* **2011**, *2* (2), 96-107. DOI: 10.1111/j.2041-1294.2011.00039.x.

6. Li, H.; Richards, C.; Watson, J. High-Performance Glass Fiber Development for Composite Applications. *International Journal of Applied Glass Science* **2014**, *5* (1), 65-81. DOI: 10.1111/ijag.12053.

7. Sathishkumar, T. P.; Satheeshkumar, S.; Naveen, J. Glass fiber-reinforced polymer composites - a review. *Journal of Reinforced Plastics and Composites* **2014**, *33* (13), 1258-1275. DOI: 10.1177/0731684414530790.

8. Zu, Q.; Huang, S.; Zhang, Y.; Huang, S.; Liu, J.; Li, H. Compositional effects on mechanical properties, viscosity, and crystallization of (Li_2O, B_2O_3, MgO)-Al_2O_3-SiO_2 glasses. *Journal of Alloys and Compounds* **2017**, *728*, 552-563. DOI: 10.1016/j.jallcom.2017.08.294.

9. Liu, W.; Pang, Z.; Wang, J.; Zuo, H.; Xue, Q. Investigation of viscosity and structure of CaO-SiO_2-MgO-Al_2O_3-BaO-B_2O_3 slag melt. *Ceramics International* **2022**, *48* (12), 17123-17130. DOI: 10.1016/j.ceramint.2022.02.268.

10. Charpentier, T.; Ollier, N.; Li, H. RE_2O_3-alkaline earth-aluminosilicate fiber glasses: Melt properties, crystallization, and the network structures. *Journal of Non-Crystalline Solids* **2018**, *492*, 115-125. DOI: 10.1016/j.jnoncrysol.2018.04.028.

11. Rog, T.; Murzyn, K.; Hinsen, K.; Kneller, G. R. nMoldyn: a program package for a neutron scattering oriented analysis of molecular dynamics simulations. *J Comput Chem* **2003**, *24* (5), 657-667. DOI: 10.1002/jcc.10243.

12. Shi, Y.; Tandia, A.; Deng, B.; Elliott, S. R.; Bauchy, M. Revisiting the Makishima-Mackenzie model for predicting the young's modulus of oxide glasses. *Acta Materialia* **2020**, *195*, 252-262. DOI: 10.1016/j.actamat.2020.05.047.

13. Bapst, V.; Keck, T.; Grabska-Barwińska, A.; Donner, C.; Cubuk, E. D.; Schoenholz, S. S.; Obika, A.; Nelson, A. W. R.; Back, T.; Hassabis, D.; et al. Unveiling the predictive power of static structure in glassy systems. *Nature Physics* **2020**, *16* (4), 448-454. DOI: 10.1038/s41567-020-0842-8.

14. Rajbhandari, P.; Montagne, L.; Tricot, G. Doping of low-Tg phosphate glass with Al_2O_3, B_2O_3 and SiO_2: Part I- effect on glass property and stability. *Materials Chemistry and Physics* **2016**, *183*, 542-550. DOI: 10.1016/j.matchemphys.2016.09.013.

15. Rajbhandari, P.; Montagne, L.; Tricot, G. Doping of low-Tg phosphate glass with Al_2O_3, B_2O_3 and SiO_2: Part II- insertion mechanism of Al_2O_3 and B_2O_3 in phosphate network characterized by 1D/2D solid-state NMR. *Materials Chemistry and Physics* **2018**, *218*, 122-129. DOI: 10.1016/j.matchemphys.2018.07.031.

16. Ren, M.; Cheng, J. Y.; Jaccani, S. P.; Kapoor, S.; Youngman, R. E.; Huang, L.; Du, J.; Goel, A. Composition-structure-property relationships in alkali aluminosilicate glasses: A combined experimental-computational approach towards designing functional glasses. *Journal of Non-Crystalline Solids* **2019**, *505*, 144-153. DOI: 10.1016/j.jnoncrysol.2018.10.053.

17. Jabraoui, H.; Badawi, M.; Lebègue, S.; Vaills, Y. Elastic and structural properties of low silica calcium aluminosilicate glasses from molecular dynamics simulations. *Journal of Non-Crystalline Solids* **2018**, *499*, 142-152. DOI: 10.1016/j.jnoncrysol.2018.07.004.

18. Weigel, C.; Le Losq, C.; Vialla, R.; Dupas, C.; Clément, S.; Neuville, D. R.; Rufflé, B. Elastic moduli of $XAlSiO_4$ aluminosilicate glasses: effects of charge-balancing cations. *Journal of Non-Crystalline Solids* **2016**, *447*, 267-272. DOI: 10.1016/j.jnoncrysol.2016.06.023.

19. Iftekhar, S.; Pahari, B.; Okhotnikov, K.; Jaworski, A.; Stevensson, B.; Grins, J.; Edén, M. Properties and Structures of RE_2O_3-Al_2O_3-SiO_2 (RE = Y, Lu) Glasses Probed by Molecular Dynamics Simulations and Solid-State NMR: The Roles of Aluminum and Rare-Earth Ions for Dictating the Microhardness. *The Journal of Physical Chemistry C* **2012**, *116* (34), 18394-18406. DOI: 10.1021/jp302672b.

20. Kalahe, J.; Stone, M. P.; Dragic, P. D.; Ballato, J.; Du, J. The structures and properties of yttrium aluminosilicate glasses with low, medium, and high silica contents. *Journal of Non-Crystalline Solids* **2023**, *614*. DOI: 10.1016/j.jnoncrysol.2023.122394.

21. Du, J.; Cormack, A. N. "Atomistic Simulations of Glasses: Fundamentals and Applications", ISBN 9781118939062, Wiley, (2022).

22. Du, J. "Challenges in molecular dynamics simulations of multicomponent oxide glasses", in "Molecular Dynamics Simulations of Disordered Materials: from Network Glasses to Phase-Change Memory Alloys", Springer Series in Material Science, Vol. 215, pp157-180, Springer, ISBN 978-3-319-15674-3 (2015).

23. Du, J. "Molecular dynamics simulations of oxide glasses", Springer Handbook of Glass, Eds. J. D. Musgraves, J. Hu, L. Calvez, Springer, pp 1129-1151 ISBN978-3-319-93726-7 (2019).

24. Yue, Y.; Tuheen, M.I.; Du, J. Borosilicate Glasses, Encyclopedia of Materials: Technical Ceramics and Glasses2021, pp. 519-539.

25. Urata, S.; Miyajima, T.; Kayaba, N.; Deng, L.; Du, J. Development of a force field for modeling lithium borosilicate glasses. *International Journal of Applied Glass Science* **2022**, *13* (3), 444-456. DOI: 10.1111/ijag.16570.

26. Deng, L.; Du, J. "Borosilicate and Boroaluminosilicate Glasses", in "Atomistic Simulations of Glasses Fundamentals and Applications", pp 224-260, John Wiley & Sons Inc. (2022).

27. Tuheen, M. I.; Deng, L.; Du, J. A comparative study of the effectiveness of empirical potentials for molecular dynamics simulations of borosilicate glasses. *Journal of Non-Crystalline Solids* **2021**, *553*, 120413. DOI: 10.1016/j.jnoncrysol.2020.120413.

28. Du, J.; Cormack, A. N. The medium range structure of sodium silicate glasses: a molecular dynamics simulation. *Journal of Non-Crystalline Solids* **2004**, *349*, 66-79. DOI: 10.1016/j.jnoncrysol.2004.08.264.

29. Deng, L.; Du, J. Development of boron oxide potentials for computer simulations of multicomponent oxide glasses. *Journal of the American Ceramic Society* **2018**, *102* (5), 2482-2505. DOI: 10.1111/jace.16082.

30. Dell, W.; Bray, P.; Xiao, S. ^{11}B NMR studies and structural modeling of Na_2O-B_2O_3-SiO_2 glasses of high soda content. *Journal of Non-Crystalline Solids* **1983**, *58*, 1-16.

31. Wang, M.; Anoop Krishnan, N. M.; Wang, B.; Smedskjaer, M. M.; Mauro, J. C.; Bauchy, M. A new transferable interatomic potential for molecular dynamics simulations of borosilicate glasses. *Journal of Non-Crystalline Solids* **2018**, *498*, 294-304. DOI: 10.1016/j.jnoncrysol.2018.04.063.

32. Kieu, L.-H.; Delaye, J.-M.; Cormier, L.; Stolz, C. Development of empirical potentials for sodium borosilicate glass systems. *Journal of Non-Crystalline Solids* **2011**, *357* (18), 3313-3321. DOI: 10.1016/j.jnoncrysol.2011.05.024.

33. Yang, R.; Zhang, Y.; Zu, Q.; Huang, S. X.; Zhang, L. Z.; Deng, L.; Zeng, H. D. Molecular dynamics simulations study on structure and properties of CaO-MgO-B_2O_3-Al_2O_3-SiO_2 glasses with different B_2O_3/MgO. *Journal of Non-Crystalline Solids* **2023**, *616*. DOI: ARTN 122458 10.1016/j.jnoncrysol.2023.122458.

34. Lobanov, M. K. a. V. S. Quantum-Chemical Descriptors in QSAR/QSPR Studies. *Chem. Rev.* **1996**, *96*, 1027-1043.

35. Linati, L.; Lusvardi, G.; Malavasi, G.; Menabue, L.; Menziani, M.; Mustarelli, P.; Segre, U. Qualitative and Quantitative Structure-Property Relationships Analysis of Multicomponent Potential Bioglasses. *J. Phys. Chem. B* **2005**, *109*, 4989-4998.

36. Lusvardi, G.M. G.; Tarsitano, F.; Menabue, L.; Menziani, M.C.; Pedone, A. Quantitative Structure-Property Relationships of Potentially Bioactive Fluoro Phospho-silicate Glasses. *J. Phys. Chem. B* **2009**, *113*, 10331-10338.

37. Lu, X.; Deng, L.; Gin, S.; Du, J. Quantitative Structure-Property Relationship (QSPR) Analysis of ZrO_2-Containing Soda-Lime Borosilicate Glasses. *The journal of physical chemistry. B* **2019**, *123* (6), 1412-1422. DOI: 10.1021/acs.jpcb.8b11108.

38. Thompson, A. P.; Aktulga, H. M.; Berger, R.; Bolintineanu, D. S.; Brown, W. M.; Crozier, P. S.; in 't Veld, P. J.; Kohlmeyer, A.; Moore, S. G.; Nguyen, T. D.; et al. LAMMPS - a flexible simulation tool for particle-based materials modeling at the atomic, meso, and continuum scales. *Computer Physics Communications* **2022**, *271*. DOI: 10.1016/j.cpc.2021.108171.

39. Deng, L.; Du, J. Development of effective empirical potentials for molecular dynamics simulations of the structures and properties of boroaluminosilicate glasses. *Journal of Non-Crystalline Solids* **2016**, *453*, 177-194. DOI: 10.1016/j.jnoncrysol.2016.09.021.

40. Sun, K.-H. Fundamental Condition of Glass Formation. *Journal of the American Ceramic Society* **1947**, *30* (9), 277-281. DOI: 10.1111/j.1151-2916.1947.tb19654.x.

41. Du, J.; Lu, X.; Gin, S.; Delaye, J. M.; Deng, L.; Taron, M.; Bisbrouck, N.; Bauchy, M.; Vienna, J. D. Predicting the dissolution rate of borosilicate glasses using QSPR analysis based on molecular dynamics simulations. *Journal of the American Ceramic Society* **2021**, *104* (9), 4445-4458. DOI: 10.1111/jace.17857.

42. Du, J.; Xiang, Y. Investigating the structure-diffusion-bioactivity relationship of strontium containing bioactive glasses using molecular dynamics based computer simulations. *Journal of Non-Crystalline Solids* **2016**, *432*, 35-40. DOI: 10.1016/j.jnoncrysol.2015.03.015.

43. Kuo, P. H.; Du, J. C. Lithium Ion Diffusion Mechanism and Associated Defect Behaviors in Crystalline $Li_{1+x}Al_xGe_{2-x}(PO_4)_3$ Solid-State Electrolytes. *J Phys Chem C* **2019**, *123* (45), 27385-27398. DOI: 10.1021/acs.jpcc.9b08390.

44. Du, J.; Xiang, Y. Effect of strontium substitution on the structure, ionic diffusion and dynamic properties of 45S5 Bioactive glasses. *Journal of Non-Crystalline Solids* **2012**, *358* (8), 1059-1071. DOI: 10.1016/j.jnoncrysol.2011.12.114.

45. Kuo, P. H.; Du, J. Effect of boron oxide on mechanical and thermal properties of bioactive glass coatings for biomedical applications. *Journal of the American Ceramic Society* **2022**, *105* (6), 3986-4008. DOI: 10.1111/jace.18391.

46. Thompson, A. P.; Plimpton, S. J.; Mattson, W. General formulation of pressure and stress tensor for arbitrary many-body interaction potentials under periodic boundary conditions. *J Chem Phys* **2009**, *131* (15), 154107. DOI: 10.1063/1.3245303.

47. Hill, R. The Elastic Behaviour of a Crystalline Aggregate. *Proc. Phys. Soc. A* **1952**, *65*, 349.

48. Keen, D. A. A comparison of various commonly used correlation functions for describing total scattering. *Journal of Applied Crystallography* **2000**, *34*, 172 - 177.

49. Tuheen, M. I.; Du, J. Structural features and rare earth ion clustering behavior in lanthanum phosphate and aluminophosphate glasses from molecular dynamics simulations. *Journal of Non-Crystalline Solids* **2022**, *578*. DOI: 10.1016/j.jnoncrysol.2021.121330.

50. Jia, B.; Li, M.; Yan, X.; Wang, Q.; He, S. Structure investigation of CaO-SiO_2-Al_2O_3-Li_2O by molecular dynamics simulation and Raman spectroscopy. *Journal of Non-Crystalline Solids* **2019**, *526*, 119695. DOI: 10.1016/j.jnoncrysol.2019.119695.

51. Atila, A.; Ghardi, E. M.; Ouaskit, S.; Hasnaoui, A. Atomistic insights into the impact of charge balancing cations on the structure and properties of aluminosilicate glasses. *Physical Review B* **2019**, *100* (14). DOI: 10.1103/PhysRevB.100.144109.

52. Shi, Y.; Neuefeind, J.; Ma, D.; Page, K.; Lamberson, L. A.; Smith, N. J.; Tandia, A.; Song, A. P. Ring size distribution in silicate glasses revealed by neutron scattering first sharp diffraction peak analysis. *Journal of Non-Crystalline Solids* **2019**, *516*, 71-81. DOI: 10.1016/j.jnoncrysol.2019.03.037.

53. Shi, Y.; Fu, Q.; Spier, C.; Vu, M.; Xie, W.; Du, J. Revealing structural role of ZrO_2 in silicate glasses from macroscale property by rigid-unit packing fraction method. *Journal of the American Ceramic Society* **2022**, *106* (3), 1795-1808. DOI: 10.1111/jace.18907.

54. Zeidler, A.; Salmon, P. S. Pressure-driven transformation of the ordering in amorphous network-forming materials. *Physical Review B* **2016**, *93* (21). DOI: 10.1103/PhysRevB.93.214204.

55. Shi, Y.; Lonnroth, N. T.; Youngman, R. E.; Rzoska, S. J.; Bockowski, M.; Smedskjaer, M. M. Pressure-induced structural changes in titanophosphate glasses studied by neutron and X-ray total scattering analyses. *Journal of Non-Crystalline Solids* **2018**, *483*, 50-59. DOI: 10.1016/j.jnoncrysol.2017.12.055.

56. Thao, N. T.; Kien, P. H.; Yen, N. V.; Hung, P. K.; Noritake, F. Study of sodium diffusion in silicate glasses. Molecular dynamics simulation. *Modelling and Simulation in Materials Science and Engineering* **2023**, *31* (8). DOI: 10.1088/1361-651X/ad0419.

57. Atila, A.; Ouaskit, S.; Hasnaoui, A. Ionic self-diffusion and the glass transition anomaly in aluminosilicates. *Physical chemistry chemical physics : PCCP* **2020**, *22* (30), 17205-17212. DOI: 10.1039/d0cp02910f.

58. Natrup, F. V.; Bracht, H.; Murugavel, S.; Roling, B. Cation diffusion and ionic conductivity in soda-lime silicate glasses. *Physical chemistry chemical physics : PCCP* **2005**, *7* (11), 2279-2286. DOI: 10.1039/b502501j.

59. Magnien, V.; Neuville, D. R.; Cormier, L.; Roux, J.; Hazemann, J. L.; de Ligny, D.; Pascarelli, S.; Vickridge, I.; Pinet, O.; Richet, P. Kinetics and mechanisms of iron redox reactions in silicate melts: The effects of temperature and alkali cations. *Geochimica et Cosmochimica Acta* **2008**, *72* (8), 2157-2168. DOI: 10.1016/j.gca.2008.02.007.

60. E. I. Kamitsos, M. A. K., and G. D. Chryssikos. Vibrational Spectra of Magnesium-Sodium-Borate Glasses. 2. Raman and Mid-Infrared Investigation of the Network Structure. *J. Phys. Chem.* **1987**, *91* (5), 1073-1079.

61. Mackenzie, A. M. J. DIRECT CALCULATION OF YOUNG'S MODULUS OF GLASS. *Journal of Non-Crystalline Solids* **1973**, *12*, 35-45.

62. Plucinski, M.; Zwanziger, J. W. Topological constraints and the Makishima-Mackenzie model. *Journal of Non-Crystalline Solids* **2015**, *429*, 20-23. DOI: 10.1016/j.jnoncrysol.2015.08.029.